



**HAL**  
open science

## $\beta(\text{L})\text{-Bi}_2\text{Mo}_2\text{O}_9$ : A new, highly active and selective, mild oxidation bismuth molybdate catalyst

J. M. M. Millet, T M N Le A, N. Guillou, E. Elkaïm, M. Aouine, T.M.N. Le,  
J.M.M. Millet

### ► To cite this version:

J. M. M. Millet, T M N Le A, N. Guillou, E. Elkaïm, M. Aouine, et al..  $\beta(\text{L})\text{-Bi}_2\text{Mo}_2\text{O}_9$ : A new, highly active and selective, mild oxidation bismuth molybdate catalyst. *Journal of Catalysis*, 2021, 408, pp.413-422. 10.1016/j.jcat.2021.06.023 . hal-03385144

**HAL Id: hal-03385144**

**<https://hal.science/hal-03385144>**

Submitted on 19 Oct 2021

**HAL** is a multi-disciplinary open access archive for the deposit and dissemination of scientific research documents, whether they are published or not. The documents may come from teaching and research institutions in France or abroad, or from public or private research centers.

L'archive ouverte pluridisciplinaire **HAL**, est destinée au dépôt et à la diffusion de documents scientifiques de niveau recherche, publiés ou non, émanant des établissements d'enseignement et de recherche français ou étrangers, des laboratoires publics ou privés.

Copyright

$\beta(\text{L})\text{-Bi}_2\text{Mo}_2\text{O}_9$ : a new, highly active and selective, mild  
oxidation bismuth molybdate catalyst.

T.M.N. Le<sup>a</sup>, N. Guillou<sup>b</sup>, E. Elkaïm<sup>c</sup>, M. Aouine<sup>a</sup>, J.M.M. Millet<sup>a\*</sup>

<sup>a</sup> Univ Lyon, Université Claude Bernard Lyon 1, CNRS, IRCELYON - UMR 5256, 2 Av.

Albert Einstein, 69626 Villeurbanne (France)

<sup>b</sup> Institut Lavoisier de Versailles, UMR 8180 CNRS, UVSQ, Université Paris-Saclay, 45 av.

des États-Unis, 78000 Versailles (France)

<sup>c</sup> Synchrotron Soleil, L'Orme des Merisiers, Saint-Aubin - BP 48

91192 Gif-sur-Yvette Cedex

\* Corresponding author: jean-marc.millet@ircelyon.univ-lyon1.fr

## Highlights

- A new bismuth molybdate  $\beta(\text{L})\text{-Bi}_2\text{Mo}_2\text{O}_9$  has been discovered and its structure solved
- This phase appears to be a low temperature polymorphic form of  $\beta\text{-Bi}_2\text{Mo}_2\text{O}_9$
- It is stable up to  $532^\circ\text{C}$  where it transforms to the known high temperature form
- Tested in propene oxidation, it is as active and selective as  $\alpha\text{-Bi}_2\text{Mo}_3\text{O}_{12}$

## Abstract

A new bismuth molybdate, obtained by means of microwave-assisted hydrothermal synthesis, is described by the chemical formula:  $\beta(\text{L})\text{-Bi}_2\text{Mo}_2\text{O}_9$ , in accordance with its low crystallization temperature and transition to  $\beta\text{-Bi}_2\text{Mo}_2\text{O}_9$  at 532°C. Its structure, solved *ab initio* using powder diffraction data, crystallizes in the monoclinic system (space group  $P2_1/c$ ), with  $a = 8.11413(5)$ ,  $b = 8.54445(5)$ ,  $c = 13.43623(6)$  Å, and  $\beta = 123.5085(2)^\circ$ . This phase has been tested as a catalyst for the oxidation of propene. It appears to be highly stable on stream, with a specific rate of propene conversion comparable to that of  $\alpha\text{-Bi}_2\text{Mo}_3\text{O}_{12}$  and a slightly higher selectivity to acrolein. A possible active site for the abstraction of the first hydrogen from propene has been identified, by analogy with that proposed for  $\alpha\text{-Bi}_2\text{Mo}_3\text{O}_{12}$  and seems to correspond to a molybdenyl Mo=O oxygen that is weakly coordinated to a neighboring Bi cation

**Keywords:** Heterogeneous catalysis, Bismuth Molybdate, Selective Oxidation of Propene, Acrolein, Bi-Mo-O system, microwave-assisted hydrothermal synthesis

## 1. Introduction

In the field of heterogeneous catalysis, few reactions have been as extensively studied, from both the academic and industrial perspectives, as the oxidation of propene to acrolein. This is due to the economic importance of the process itself, since acrolein is the key intermediate in the production of both acrylic acid and methionine, and because the catalysts which, over the last sixty years have been developed for this reaction, have also served as model for reaction involving the so-called Mars and van Krevelen mechanism [1]. A major breakthrough was achieved in the search for active and selective catalysts for this reaction in 1957, following the discovery by Callahan and coworkers of the  $\text{Bi}_2\text{O}_3\text{-MoO}_3$  catalyst, which functions under oxygen-rich conditions [2,3]. Moreover, this type of catalyst also performs extremely well in other reactions, such as the ammoxidation of propene and the oxidative dehydrogenation of 1-butene to butadiene, which led to a further boost to the industrial and academic interest for this system.

Soon after this discovery, it was shown that the properties of the  $\text{Bi}_2\text{O}_3\text{-MoO}_3$  catalyst were related to the formation of mixed bismuth and molybdenum oxides. In these Bi-molybdates, Bi is responsible for  $\alpha$ -hydrogen abstraction of the propene molecule and Mo for the chemisorption of radicals and the insertion of O, with Bi and Mo having to be adjacent to each other [4-6]. Recent studies have provided an accurate description of the involvement of these two elements, and the reaction steps that take place [7,8]. Three phases appear to be of significance for catalysis:  $\alpha\text{-Bi}_2\text{Mo}_3\text{O}_{12}$ ,  $\beta\text{-Bi}_2\text{Mo}_2\text{O}_9$  and  $\gamma\text{-Bi}_2\text{MoO}_6$ . Although most current industrial catalysts contain the  $\alpha\text{-Bi}_2\text{Mo}_3\text{O}_{12}$  phase only as active phase, it is generally reported that the  $\beta$ -phase catalytically outperforms the other phases [4,9-11]. However, this phase can be accessed only at high temperatures, is unstable under catalytic reaction conditions involving lengthy on-stream processes, and

decomposes into the  $\alpha$ - and  $\gamma$ -phases. It has been proposed that this decomposition contributes to the catalyst's high efficiency, since a synergetic interaction occurs between the  $\alpha$ - and  $\beta$ - or  $\gamma$ -phases [12-14]. This synergy has been ascribed to the oxygen's mobility in the lattice of the  $\gamma$ -phase, which promotes the migration of oxygen species from the  $\gamma$  to the other phases, similarly to the migration observed between iron and cobalt molybdate and bismuth molybdates [15]. It thus appears that the purity of the phases is an important parameter, having an influence on their relative levels of activity. The debate on the most active and selective phase is thus not settled, especially since other studies suggest that either  $\alpha$ - or  $\gamma$ -phases are the most active [16,17]. Moreover, in the case of the  $\gamma$ -phase it has been reported that an excess of bismuth may be present on its surface, depending upon the synthesis technique, which may modify its catalytic properties [12,18]. Nevertheless, whatever the active phase for this type of catalyst, it should have optimal properties of oxygen mobility, Bi-Mo separation and Bi and Mo coordination at its surface. The "ideal catalyst" would also have optimal bulk properties, such as electron storage capacity and oxygen vacancy content. Due to these high requirements, for many years researchers have been unable to come up with a new high performance active phase for bismuth molybdate catalysts.

In this paper we report the synthesis and characterization of a new binary bismuth molybdate catalyst, which was obtained using a microwave-assisted hydrothermal method. Although a large number of techniques have been used to synthesize bismuth molybdates over the years, this one has never been reported before [19]. The synthesis parameters were optimized, and the structure of this new low-temperature phase was determined *ab initio* from powder X-ray diffraction data. Its physicochemical characteristics and catalytic properties for the oxidation of propene to acrolein were studied and compared to those of other known bismuth molybdates.

## 2. Materials and methods

$\beta(\text{L})\text{-Bi}_2\text{Mo}_2\text{O}_9$  has been synthesized using a microwave-assisted hydrothermal method, which has recently been shown to be well suited for the synthesis of molybdates [20]. Firstly, 15g of  $\text{Bi}(\text{NO}_3)_3 \cdot 5\text{H}_2\text{O}$  (Bi= 30 mmol, Sigma-Aldrich 10035-06-0) was dissolved in 300 mL of distilled water by adding 15 mL of  $\text{HNO}_3$  65%. Separately, 5.296 g of  $(\text{NH}_4)_6\text{Mo}_7\text{O}_{24} \cdot 4\text{H}_2\text{O}$  (Mo = 30 mmol, Sigma-Aldrich 12054-85-2) was dissolved in 200 mL of distilled water. The mixture solution with its white precipitate was maintained at room temperature under stirring and the pH was adjusted to 1.0 by adding  $\text{NH}_4\text{OH}$  32% solution. The solution was then transferred in a 30 mL-glass reactor for Monowave 300 (Anton Paar) or 1L-Teflon reactor for SynthWAVE (Milestone) microwave apparatus and heated with a maximum of 1500 W in 5 min at  $175^\circ\text{C}$ . In the first instrument, a fiber optic probe sensor based on the temperature-dependent luminescence of a ruby crystal was used for accurate temperature monitoring in microwaves environment. In the second one, a protected downward Pt probe was used. The solution was maintained at this temperature for 20 min under stirring (600 rpm) and cooled down to room temperature. The solid product was recovered by high-speed centrifugation, washed several times with water and then dried at  $100^\circ\text{C}$  overnight.

The two other bismuth molybdates,  $\alpha\text{-Bi}_2\text{Mo}_3\text{O}_{12}$  and  $\gamma\text{-Bi}_2\text{MoO}_6$ , have been synthesized for comparison using the same technique. Same starting solutions containing the precursors were prepared, but in the appropriate relative Bi/Mo ratios and with pH systematically adjusted by adding  $\text{NH}_4\text{OH}$  32% solution, at 1.0 and 8.0, respectively. The high temperature form of  $\beta\text{-Bi}_2\text{Mo}_2\text{O}_9$ , further named  $\beta(\text{H})\text{-Bi}_2\text{Mo}_2\text{O}_9$  has been prepared by calcining the  $\beta(\text{L})\text{-Bi}_2\text{Mo}_2\text{O}_9$  phase at  $560^\circ\text{C}$  in air for 4 hours.

Chemical analysis of the solids was performed using an ACTIVA JOBIN YVON atomic emission spectrophotometer (ICP-AES). For that purpose, the solids (10 mg) were solubilized in an aqueous solution (100 mL) containing HF (5 mL), H<sub>2</sub>SO<sub>4</sub> (5 mL), and HNO<sub>3</sub> (5 mL) at 200°C with stirring for 6 h. The specific surface areas were measured by nitrogen physisorption at -196°C using a Micromeritics ASAP 2020 instrument and applying the Brunauer-Emmett-Teller (BET) method after degassing at 250°C under primary vacuum for 2 h. Thermal and thermogravimetric analyses (DTA-TGA) were performed with a TGA/DSC 1 STARe System from Mettler Toledo. About 10 mg of samples were placed in a platinum crucible and heated under air at a 5°C min<sup>-1</sup> rate.

Routine X-Ray Diffraction (XRD) data were collected with a Bruker D8A25 X-ray diffractometer operating at 50 kV and 35 mA and selected Cu K $\alpha$  radiation at 1.54184 Å. The diffracted intensities were measured using a LynxEye, 192 channels on 2.95°) fast multistrip detector. Diffraction patterns were collected at 25°C in the 4-80° 2 $\theta$  range with 0.02° 2 $\theta$  step size and 2 s per step and compared to the calculated ones from the ICSD database. *In situ* powder X-ray diffraction was performed as previously described [21]. Samples were mounted in a controlled atmosphere (air flow) cell and heated from room temperature to 485°C. Patterns were then recorded each 15°C after stabilization up to 550°C.

For the structural determination, high resolution XRD data were collected on the CRISTAL beamline at Soleil Synchrotron (Gif-sur-Yvette, France). A monochromatic beam was extracted from the U20 undulator beam by means of a Si(111) double monochromator. Its wavelength of 0.7289 Å was refined from a LaB<sub>6</sub> (NIST Standard Reference Material 660a) powder diagram recorded prior to the experiment. High angular resolution was obtained with, in the diffracted beam, a 21 perfect crystal Si(111) multi-analyzer. The sample was

loaded in a 0.3 mm capillary (Borokapillaren, GLAS, Schönwalde, Germany) mounted on a spinner rotating at about 5 Hz to improve the particles' statistics. Two Diffraction data were collected in continuous scanning mode in about 30 min and the diffractogram was obtained from the precise superposition and addition of the 21 channels data.

All steps of the *ab initio* structural determination from powder diffraction were carried out with the Topas V5 Bruker AXS Ltd 2014 software : extractions of the peak positions, pattern indexing, charge flipping, simulated annealing processes, Fourier difference calculations and Rietveld refinements.

Surface composition was analyzed by X-ray photoelectron spectroscopy (XPS) using Al K $\alpha$  monochromatized source in a commercial KRATOS AXIS Ultra DLD spectrometer. XPS high resolution spectra revealed well-resolved chemical states corresponding to Bi 2p, Mo 3d, O 1s and C 1s levels. Each core level was decomposed into a combination of Voigt functions with an overall FWHM of around 1.6 eV. For the study, samples have been characterized before and after catalytic testing. Raman spectroscopy was performed using a JOBIN-YVON LabRam Infinity apparatus equipped with a CCD detector operating at liquid nitrogen temperature. A D2 filter was used to protect the catalyst structure from destruction by the laser (wavelength  $\lambda=520$  nm). The Raman shift was recorded in the range of 200-5500  $\text{cm}^{-1}$ . The homogeneity of the samples was evaluated by performing the analysis on at least three different locations for each sample. UV-vis diffuse reflectance spectra of the bismuth molybdates were recorded with an optical probe connected to an Avantes AvaSpec-2048 UV-vis spectrometer. BaSO<sub>4</sub> was used as standard reference. It is assumed that the absorption coefficient  $\alpha$  is weakly dependent on the scattering coefficient S on the wavelength, therefore, the absorption coefficient  $\alpha$  is proportional to K/S and was calculated using the Schuster-Kubelka-Munk relation. Band gap energy value was calculated according to the UV-Vis DRS

spectrum and equation:  $(\alpha h\nu)^{1/2} = A(h\nu - E_g)$  where  $\alpha$ ,  $\nu$ ,  $E_g$  and  $A$  are respectively the absorption coefficient, the photonic frequency, the band gap energy and a constant.

Sample preparation for scanning electron microscopy (SEM) analysis included sonicating a dilute suspension of the nanomaterial in water or methanol for 20 - 30 minutes and dropping a portion onto an aluminum SEM stub with a pipette. Once the droplet was dry, SEM analysis was performed in high vacuum conditions on an ESEM-FEG FEI XL 30 microscope, using secondary electrons for imaging purposes. The samples were then coated with a film of sputtered gold in order to avoid charging effects. High resolution images of the solid were obtained by transmission electron microscopy (TEM) using a FEI TITAN ETEM G2 microscope, operating at 300 KV and equipped with an objective Cs aberration corrector. The sample preparation technique developed for molybdates has been described previously [22]. In parallel, an energy-dispersive X-ray (EDX) analyzer (SDD X-Max 80mm<sup>2</sup> from Oxford Instruments TM) was used to acquire elemental chemical analysis and verify the stoichiometry of the phase.

The synthesized solids were tested in the oxidation of propene to acrolein at atmospheric pressure between 320 and 380°C in a fixed-bed type reactor. The reactant and the products of the reaction were analyzed on-line by chromatography [23, 24]. The quartz reactor contained 0.2 to 2.0 g of powdered solid previously sieved below 180  $\mu\text{m}$ . The reaction temperature was measured with a thermocouple positioned in the catalyst bed supported on a sintered glass. The high purity gases used as carrier or reactant were purchased from Air Liquid. The starting reaction mixture corresponded to  $\text{C}_3\text{H}_6/\text{O}_2/\text{N}_2 = 1: 1.5: 8.6$  and the total gas flow was equal to 60 ml min. Calculated carbon balances were higher than 98%. The catalysts were directly heated to the catalytic reaction temperature under nitrogen. The catalytic gas

mixture was introduced and the first analyzed were performed half an hour later. The catalysts were tested for periods of  $24 \pm 2$  h except  $\beta(\text{L})\text{-Bi}_2\text{Mo}_2\text{O}_9$ , which was tested for 72 h. Conversion of propene (A) was calculated using  $\text{N}_2$  as internal standard as :

$$X(A) = \frac{\text{moles A before reaction} - \text{moles A after reaction}}{\text{moles A before reaction}} \cdot 100$$

This conversion was systematically lower than 5%, and the reactor was considered differential. The selectivity for a reaction product (B) (acrolein,  $\text{CO}_2$ , acrylic acid and acetaldehyde) was defined as the ratio between the moles of (B) produced during the reaction, over the moles of the reagent (A) present before the reaction corrected by the carbon atoms number in product (B) and reactant (A) as:

$$S(B) = \frac{\text{moles B after reaction}}{(\text{moles A before reaction} - \text{moles A after reaction})} \frac{\text{carbon atom B}}{\text{carbon atom A}} \cdot 100$$

The rate equation for calculating the propene initial rate ( $-r(A)$ ) was based on a first order reaction and calculated using the following equation :

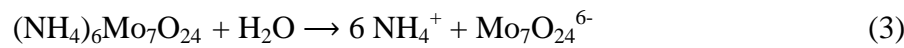
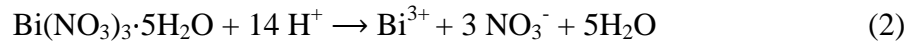
$$-r(A) = \frac{Fa_0 X(A)}{ms} \quad (1)$$

where :  $Fa_0$  is the inflow rate of propene ( $\text{mol} \cdot \text{s}^{-1}$ ),  $m$  is the mass of the catalyst (g) and  $s$  is the surface are of the catalyst ( $\text{m}^2 \cdot \text{g}^{-1}$ )  $x$  is the conversion of propene.

### 3. Results and discussion

The synthesis protocol described in the experimental section made it possible to crystallize a phase, which does not correspond to any of the previously described compounds of the  $\text{Bi}_2\text{O}_3\text{-MoO}_3$  phase diagram. Chemical analysis of the resulting solid led to a Bi/Mo ratio of 1.02.

Since it was prepared at low temperatures, this new phase has been named  $\beta(\text{L})\text{-Bi}_2\text{Mo}_2\text{O}_9$ , which matches the nominal composition. The known phase with the same composition, but which is stable only at high temperatures, is referred as  $\beta(\text{H})\text{-Bi}_2\text{Mo}_2\text{O}_9$ . The requirements for the successful preparation of molybdates are extremely critical, in particular the pH [20]. At pH=1, the stable species are, in the case of bismuth:  $\text{Bi}^{3+}$  or  $\text{Bi}(\text{OH})^{2+}$ ; and in the case of molybdenum:  $\text{H}_2\text{MoO}_4$  [25, 26]. Both monomeric species should react and the following equations can be proposed for the solubilization and precipitation reactions leading to the formation of the  $\beta(\text{L})\text{-Bi}_2\text{Mo}_2\text{O}_9$  phase:



In order to optimize the crystallization process and to determine whether the  $\beta(\text{L})\text{-Bi}_2\text{Mo}_2\text{O}_9$  phase could be obtained with a different texture, several synthesis parameters were studied. Synthesis temperatures ranging between 150 and 175°C and reaction times ranging between 10 and 30 min were tested. The dilution of the precursors in the starting solution was modified, and the solvent was changed from water to an equimolar mixture of water and ethylene glycol and pure ethylene glycol, while leaving the other parameters unchanged. The reaction temperature and time have almost no influence on the resulting solid, over the temperature range used in the study. When the aqueous dilution of the precursors was increased, the resulting solid was unchanged, but its specific surface area slightly increased, from around 2 to a maximum of 8  $\text{m}^2 \text{g}^{-1}$  (Fig. S1). When the solvent was changed to a mixture of water and ethylene glycol, the resulting solid contained a mixture of  $\beta(\text{L})\text{-}$  and  $\gamma\text{-}$  phases, whereas a pure ethylene glycol solvent led to the production of the  $\gamma\text{-}$  phase solely

(Fig. S2). In the latter case, the X-ray diffraction peaks were broader, which can be explained by the influence of the solvent on the size of the crystallites. This effect was expected, since polyols are known to act not only as solvents, but also as stabilizers in this process, by restricting particle growth and preventing agglomeration [27-29]. This decrease in particle size was confirmed through measurements of the specific surface area of the phase, which increased to  $73 \text{ m}^2 \text{ g}^{-1}$ . However, the observed influence of the solvent on the nature of the phases produced by the process was unexpected. One hypothesis is that, during the course of the reaction in ethylene glycol, bismuth is easily complexed by an asymmetric bidentate ethane-1,2-diolato(2-) ligand [30-32]. The dimeric heteroleptic-alkoxide complexes, that are similarly formed with di, tri, tetra, penta and even hexaethylene glycol, could be first-choice precursors for  $\gamma\text{-Bi}_2\text{MoO}_6$ . The following chemical equations are proposed for the formation of the  $\gamma\text{-Bi}_2\text{MoO}_6$  phase:



Crystals of  $\beta(\text{L})\text{-Bi}_2\text{Mo}_2\text{O}_9$  obtained in water under standard conditions have an anisotropic morphology, with a platelet-like crystal habit (Fig. 1). The average length of the crystals is  $\sim 3\text{-}4 \mu\text{m}$ , with an average width of  $\sim 1\text{-}2 \mu\text{m}$  and a thickness of approximately  $0.4 \mu\text{m}$ , which is too small for a structural determination to be performed from single crystal data. For this reason, an *ab initio* structural determination was undertaken using powder diffraction data .

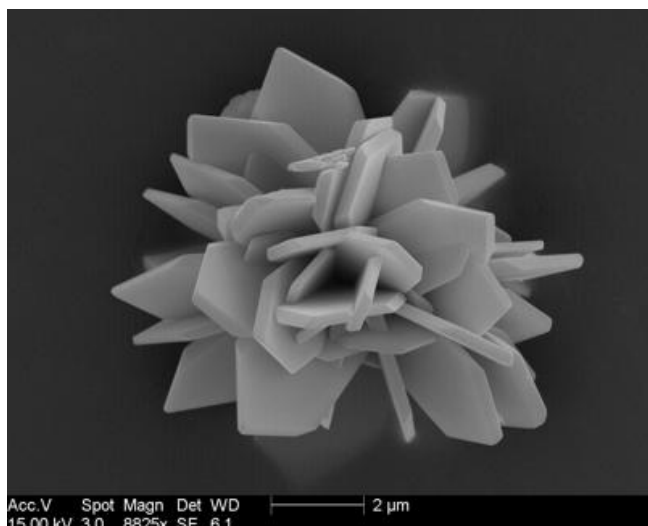


**Fig 1** SEM image of the  $\beta(L)$ - $\text{Bi}_2\text{Mo}_2\text{O}_9$  phase.

The LSI-indexing method, based on the first 20 diffraction peaks, converged unambiguously to a monoclinic unit cell with a satisfactory figure of merit (see Table 1).  $\beta(L)$ - $\text{Bi}_2\text{Mo}_2\text{O}_9$  crystallizes in the monoclinic system (space group:  $P2_1/c$ ) with  $a = 8.11413(5)$ ,  $b = 8.54445(5)$ ,  $c = 13.43623(6)$  Å and  $\beta = 123.5085(2)^\circ$ . The charge-flipping method allowed the Bi and Mo cations to be unambiguously localised, following which their atomic coordinates were used as a starting model for the Rietveld refinement. Assuming that all Mo cations were tetrahedrally coordinated, and treating them as rigid bodies in a simulated annealing process with only refining their orientation, the direct space strategy was then used to complete the structural model. Finally, successive difference Fourier map computations revealed that the environments of the Mo cations were in fact square pyramids, connected by sharing edges and allowed to locate and additional oxygens only connected to Bi cations.

At the final stage of the Rietveld refinement, all atoms were treated independently. This involved the following structural parameters: 1 scale factor, 39 atomic coordinates and 3 thermal factors for 1686 reflections. The anisotropic line-broadening effect was modeled using the Stephens model. The final Rietveld plot (Fig. 2) is characterized by a satisfactory model indicator ( $R_{\text{Bragg}} = 0.018$ ) and profile factors ( $R_{\text{p}} = 0.053$  and  $R_{\text{wp}} = 0.073$ ).

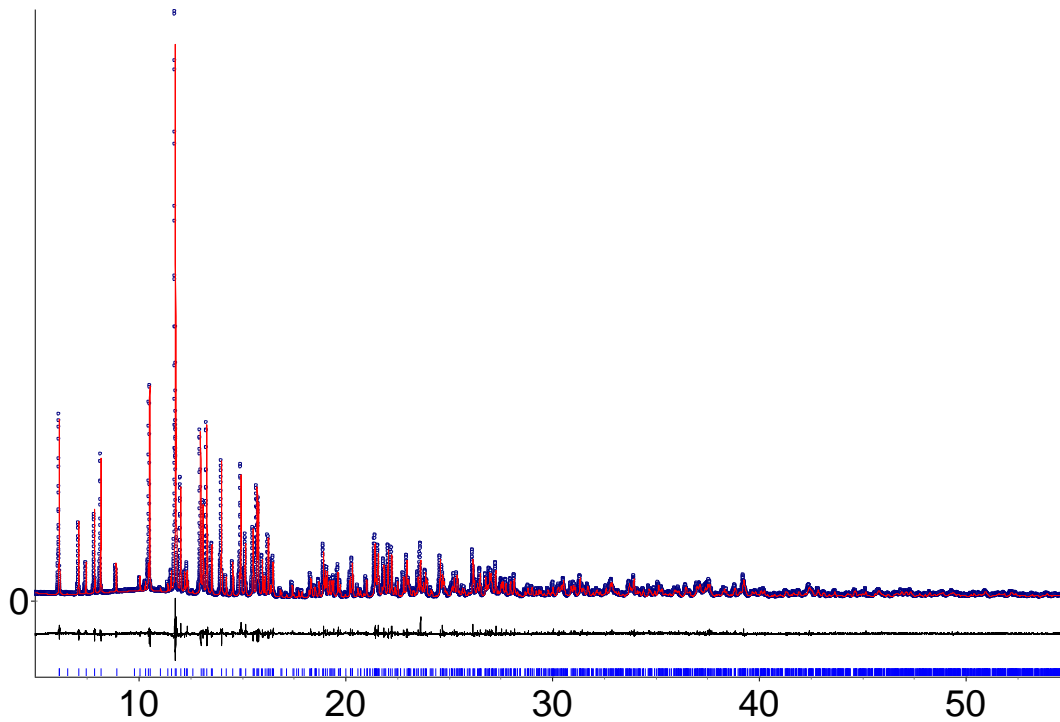


**Fig. 2** Final Rietveld plot for  $\beta(L)\text{-Bi}_2\text{Mo}_2\text{O}_9$ . The observed data are denoted by blue dot symbols, and the computed ones are represented by the continuous red line. The bottom line corresponds to the difference curve and the blue marks to the Bragg positions

The platelet axis coincides with the  $(010)$ -axis (Fig. 3). The specific surface area is comparable to that of other bismuth molybdates, prepared using different methods. Like most of the bismuth molybdate phases, the structure is derived from that of a fluorite, with vacant metal sites and a sub-cell lattice constant of approximately 0.58 nm (Fig. 3).

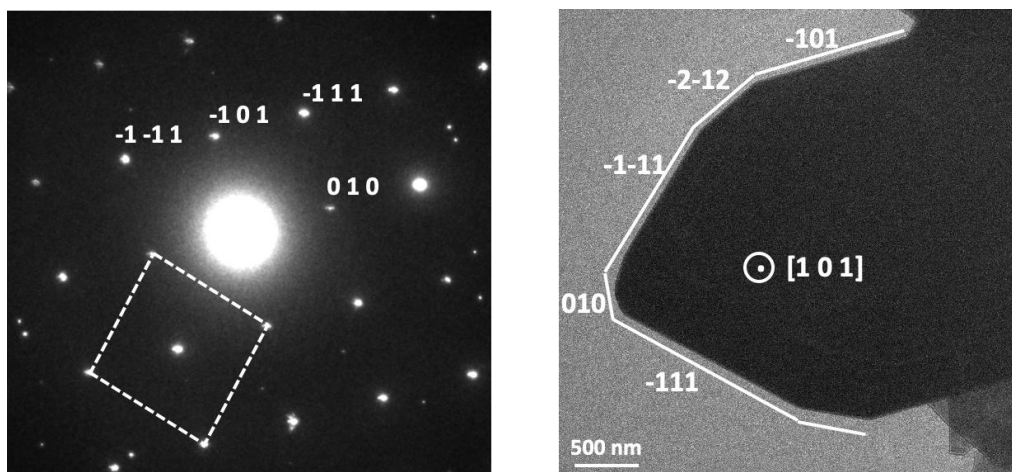


**Fig. 3** TEM image of a platelet of  $\beta(L)\text{-Bi}_2\text{Mo}_2\text{O}_9$ , showing its faceting and the indexed electron diffraction pattern. A fluorite sub-cell is indicated by the dotted lines.

Crystal and X-ray analysis data of the title compound are summarized in Table 1.

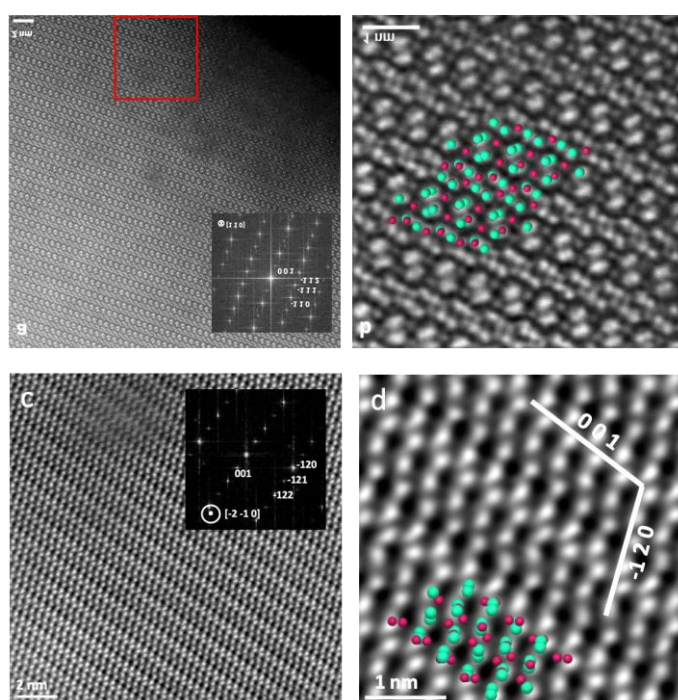


**Fig. 4** Atomic resolution HAADF image of the new phase, along the  $[110]$  zone axis (a,b) and the  $[-2-10]$  zone axis (c,d) at low-magnification. The indexed electron diffraction patterns (a and c) are shown at high-resolution, with a superimposed view of the computed schematic model (b and d).

**Table 1:** Crystal data and Rietveld refinement parameters.

Empirical formula	Bi <sub>2</sub> Mo <sub>2</sub> O <sub>9</sub>
<i>Mr</i>	753.84
Crystal system	monoclinic
Space group	<i>P</i> 2 <sub>1</sub> / <i>c</i>
<i>a</i> (Å)	8.11413(5)
<i>b</i> (Å)	8.54445(5)
<i>c</i> (Å)	13.43623(6)
$\beta$ (°)	123.5085(2)
<i>V</i> (Å <sup>3</sup> )	776.725(7)
<i>M</i> <sub>20</sub>	425
<i>Z</i>	4
$\lambda$ (Å)	0.7289
No. struct. parameters	43
No of reflexions	1686
<i>R</i> <sub>p</sub> , <i>R</i> <sub>wp</sub>	0.053, 0.073
<i>R</i> <sub>Bragg</sub> , GoF	0.018, 1.70

The crystal structure of  $\beta$ (L)-Bi<sub>2</sub>Mo<sub>2</sub>O<sub>9</sub>, shown in Fig. 5, is constructed from two independent Mo(VI) and two independent Bi(III) cations. Each Mo(VI) cation has a distorted square pyramid coordination and is connected to its equivalent through sharing edge to form Mo<sub>2</sub>O<sub>8</sub> dimers. Mo<sub>1</sub> presents three short Mo-O distances (1.73(1) (O<sub>4</sub>), 1.74(1) (O<sub>2</sub>) and 1.81(1) Å (O<sub>3</sub>)), and two longer ones (2.02(1) Å (O<sub>5</sub>)), whereas Mo<sub>2</sub> is even more distorted with two short distances (1.71(1) Å (O<sub>7</sub> and O<sub>8</sub>)), two intermediate ones (1.91(1) (O<sub>6</sub>) and 1.916(9) Å (O<sub>9</sub>)) and a very long one (2.186(7) Å (O<sub>9</sub>)). Interestingly the same type of Mo<sub>2</sub>O<sub>8</sub> dimers are present in the in  $\alpha$ -Bi<sub>2</sub>Mo<sub>3</sub>O<sub>12</sub> whereas discrete tetrahedra exist in  $\beta$ (H)-Bi<sub>2</sub>Mo<sub>2</sub>O<sub>9</sub> and  $\gamma$ -Bi<sub>2</sub>MoO<sub>6</sub> [33-35]. Considering distances less than 3 Å, the two independent Bi(III) cations are sevenfold coordinated, with distances in the range 2.117(8)-2.908(7) Å. They form slightly distorted diamond shape tetramers constructed from two Bi<sub>1</sub> and two Bi<sub>2</sub> cations strongly connected through two O<sub>1</sub> atoms, which are at the center of triangles constructed from two Bi<sub>1</sub> and one Bi<sub>2</sub> cations. These tetramers are then arranged like a herringbone and are connected to four neighbors to form layers in the *bc* plane. The same kind of tetramers is

observed in the  $\beta(\text{H})\text{-Bi}_2\text{Mo}_2\text{O}_9$ , which crystallizes in the same space group as  $\beta(\text{L})\text{-Bi}_2\text{Mo}_2\text{O}_9$ , with a doubling of the unit cell volume. Indeed, in the case of the high-temperature form, Bi(III) cations are stacked along the  $b$  axis in two types of tunnels delimited by  $\text{MoO}_4$  tetrahedra, half of them being occupied by these kinds of tetramers. Instead of discrete as in the low temperature form, they are connected to each other and condense to form Bi(III) square columns along the  $b$  axis. Bond valence calculations [36] leads to values of 2.97, 3.11, 5.93 and 5.85 for  $\text{Bi}_1$ ,  $\text{Bi}_2$ ,  $\text{Mo}_1$  and  $\text{Mo}_2$ , respectively. Bond valence sum of  $\text{O}_4$  (1.72) clearly indicates lower bonding, whereas those of  $\text{O}_1$  and  $\text{O}_5$  (2.22 and 2.18, respectively) indicate over-bonding.

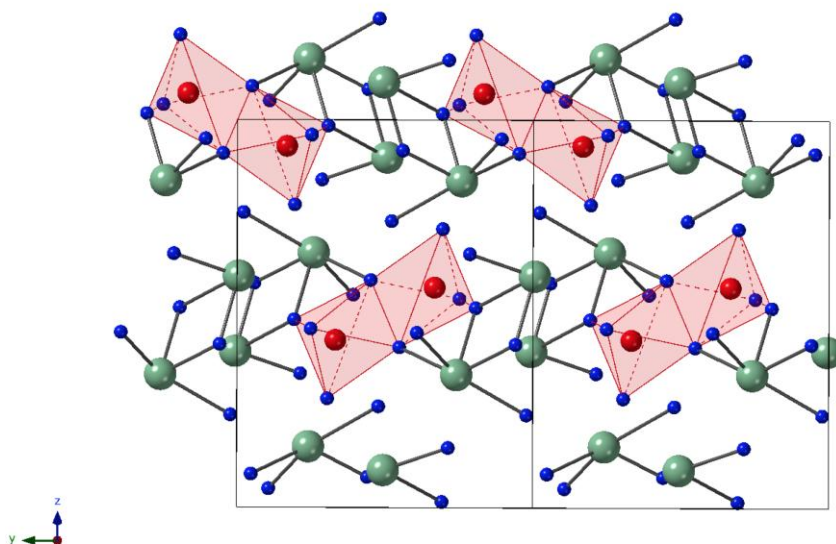


**Fig. 5** Projection of the structure of  $\beta(\text{L})\text{-Bi}_2\text{Mo}_2\text{O}_9$  along the  $a$  axis.

Finally, the resulting model was compared with the high-angle, annular dark-field images obtained using scanning transmission electron microscopy (HAADF STEM) (Fig. 4). These images reveal a well-crystallized structure, without defect, which matched well the model. All analyses by TEM never allowed to detect any particles which composition (EDX) or structure (electron diffraction or HRTEM images) would have been different from that of the new phase.

TG/DTA analysis of  $\beta(\text{L})\text{-Bi}_2\text{Mo}_2\text{O}_9$  shows that there is no mass loss and reveals the presence of only two endothermic peaks on the DTA curve at 532°C and 684 °C (Fig. 6). The first one corresponds to the phase transition to  $\beta(\text{H})\text{-Bi}_2\text{Mo}_2\text{O}_9$ , and the second to a peritectic reaction, which forms  $\alpha\text{-Bi}_2\text{Mo}_3\text{O}_{12}$ , similarly to that reported in the literature [37]. The attribution of the DTA signal to the phase transition has been confirmed by *in situ* XRD, which allowed observing the beginning of the transition in the cell between 500 and 515°C (Fig. S3). Interestingly, the phase transition temperature corresponds to that reported for the low stability limit of the  $\beta(\text{H})\text{-Bi}_2\text{Mo}_2\text{O}_9$  phase [37, 38]. Transition to the high temperature phase takes place with no significant change in crystallite morphology, apart from smoothing of the particles' surfaces, which is indicative of a small degree of sintering (Fig. S4).

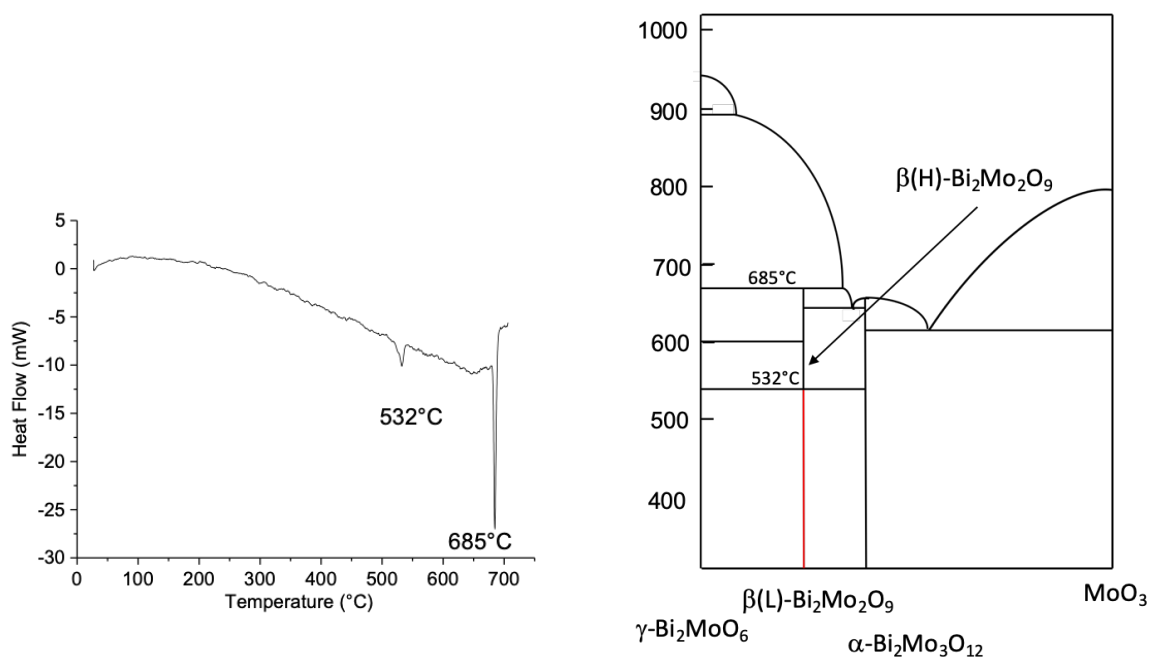


**Fig 6** DTA analysis curve of the  $\beta(\text{L})\text{-Bi}_2\text{Mo}_2\text{O}_9$  phase recorded in air ( $10 \text{ mL min}^{-1}$ ) at  $5 \text{ }^\circ\text{C min}^{-1}$ , and new phase diagram of the  $\gamma\text{-Bi}_2\text{MoO}_6\text{-MoO}_3$  binary system.

This newly reported bismuth molybdate phase was characterized by Raman spectroscopy, along with the other bismuth molybdates synthesized by the process. The spectra reveal Bi-O and Mo-O vibrations between 400 and 1000  $\text{cm}^{-1}$ , which are also visible in the IR spectrum. The Mo-O vibrations are observed between 600 and 1000  $\text{cm}^{-1}$  (Fig. 7). The same spectra as those reported in the literature are obtained for  $\alpha\text{-Bi}_2\text{Mo}_3\text{O}_{12}$ ,  $\beta(\text{H})\text{-Bi}_2\text{Mo}_2\text{O}_9$  and  $\gamma\text{-Bi}_2\text{MoO}_6$  [39-41]. On the other hand, a new and totally different spectrum is obtained for  $\beta(\text{L})\text{-Bi}_2\text{Mo}_2\text{O}_9$ . The observed Raman bands of this new phase are listed in Table 3.

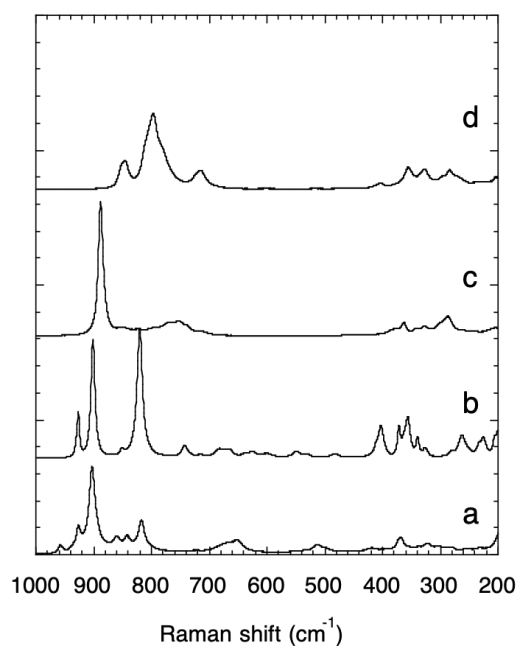


**Fig. 7:** Raman spectra of the synthesized phases: (a)  $\gamma\text{-Bi}_2\text{MoO}_6$ , (b)  $\beta(\text{L})\text{-Bi}_2\text{Mo}_2\text{O}_9$ , (c)  $\beta(\text{H})\text{-Bi}_2\text{Mo}_2\text{O}_9$  and (d)  $\alpha\text{-Bi}_2\text{Mo}_3\text{O}_{12}$ .

**Table 3** Summary of The Raman band positions of  $\beta(\text{L})\text{-Bi}_2\text{Mo}_2\text{O}_9$ 

Phase	Band position <sup>a</sup> ( $\text{cm}^{-1}$ )
$\beta(\text{L})\text{-Bi}_2\text{Mo}_2\text{O}_9$	927 (m), 902 (vs), 850 (w), 820 (vs), 742 (w), 680 (w), 668 (w), 635 (w), 624 (w), 599 (w), 548 (w), 531 (w), 484 (w), 403 (m), 372 (m), 357 (m), 339 (w), 326 (w), 279 (vw, sh), 263 (w), 226 (w), 200 (w), 160 (s), 156 (s), 133 (m, sh), 125 (m), 98 (vs), 84 (s, )78 (s), 72 (m, sh), 67 (m, sh), 61 (w,sh), 50 (m)

<sup>a</sup> Key: vw =very weak; w = weak; m = medium; s = strong; vs = very strong; sh = shoulder; br =broad.

Peaks below  $620 \text{ cm}^{-1}$  arise due to (Bi-O,  $\text{Mo}_2\text{O}_2$ ) and Mo–O bend/wag, and external modes including translational and vibration modes. Empirical relationships have been established between the metal-oxygen Raman stretching frequencies and the metal-oxygen bond lengths, for several transition-metal oxide systems [42] and a similar empirical assignment has been completed for the Mo-O bonds in  $\beta(\text{L})\text{-Bi}_2\text{Mo}_2\text{O}_9$  (Table S1). Although it is difficult to unequivocally attribute each band to a specific bond length, the lengths of the connections determined by the crystallographic study appear to correlate well with the wavelengths of the different vibrations.

The UV-vis diffuse reflectance spectrum of the  $\beta(\text{L})\text{-Bi}_2\text{Mo}_2\text{O}_9$  phase has been recorded and compared to those of the other bismuth molybdates (Fig. S5). The spectrum exhibited an intense absorption band around 360 nm, slightly higher than for  $\gamma\text{-Bi}_2\text{MoO}_6$  and  $\alpha\text{-Bi}_2\text{Mo}_3\text{O}_{12}$  at 328 nm. The estimated band gap energy  $E_g$  was equal to 2.78 eV in between those of  $\gamma\text{-Bi}_2\text{MoO}_6$  (2.60 eV) and  $\alpha\text{-Bi}_2\text{Mo}_3\text{O}_{12}$  (3.08 eV). The obtained values for the two last compounds were in good agreement with the literature [43]. These results presume possible valuable photocatalytic properties for the  $\beta(\text{L})\text{-Bi}_2\text{Mo}_2\text{O}_9$  phase if other properties like dielectric character can be added.

The catalytic properties of the new phase, in the oxidation of propene, have been determined and compared with those of the other known bismuth molybdates (Table 4). The reaction was carried out under the conditions described in the experimental section, at atmospheric pressure and under isothermal conditions ranging between 320 and 400 °C. The feedstock composition was  $C_3H_6/O_2/N_2 = 1: 1.5: 8.6$ . These conditions were chosen in order to systematically maintain the propene conversion below 5%, in order to avoid any mass or heat transfer limitations and to minimize any effects resulting from secondary reactions.

**Table 4.** Comparison of the catalytic properties of  $\beta(L)$ - $Bi_2Mo_2O_9$ , with those of other bismuth molybdates after  $24\pm 2$ h on stream. Total gas flow = 60 ml min, T = 350°C and  $C_3H_6/O_2/N_2 = 1/1.5/8.6$ . Acro : acrolein, AcrA : acrylic acid, AcA : Acetic acid

Phase	Mass of catalyst (g)	SSA ( $m^2 g^{-1}$ )	Conversion (%)	Selectivity (%)				Rate of propene conversion ( $10^{-8} mol m^{-2} s^{-1}$ )
				Acro	AcrA	AcA	CO <sub>2</sub>	
$\beta(L)$ - $Bi_2Mo_2O_9$	1.00	1.8	2.9	79.3	1.9	11.4	7.4	6.49
$\beta(H)$ - $Bi_2Mo_2O_9$	0.81	2.0	2.0	79.1	1.7	9.7	9.5	4.96
$\alpha$ - $Bi_2Mo_3O_{12}$	0.25	7.2	3.2	72.7	1.9	5.8	19.6	7.11
$\gamma(L)$ - $Bi_2MoO_6$	0.58	6.5	0.4	51.9	21.3	10.1	16.7	0.41

The same reaction products were observed on all the catalysts. In addition to acrolein, acrylic acid, acetaldehyde and CO<sub>2</sub> were formed. Although  $\alpha$ - $Bi_2Mo_3O_{12}$  is the most active phase,  $\beta(L)$ - $Bi_2Mo_2O_9$  has almost the same level of activity. On the other hand, the latter is the most selective, with a selectivity comparable to that of the high-temperature phase:  $\beta(H)$ - $Bi_2Mo_2O_9$ . The catalytic properties of all the phases were stable with time on stream in particular those of the  $\beta(H)$ - $Bi_2Mo_2O_9$  phase, that was reported not to be stable under reaction conditions; it cannot be excluded that the testing time (24h) was too short to observe any deactivation. The new phase, was tested for a longer time (72h), and did not show any

significant change in both rate of propene conversion nor selectivity to acrolein (Table S2). No transformation was detected neither by X-ray diffraction nor by XPS spectroscopy (Fig. S6 and S7). The  $\beta(\text{L})\text{-Bi}_2\text{Mo}_2\text{O}_9$  phase was also tested at different temperatures, and its acrolein selectivity was found to decrease slightly with increasing temperature. The catalyst's apparent activation energy of acrolein formation was computed as  $45 \pm 2 \text{ kcal mol}^{-1}$ , which is comparable to the values generally observed for the other known bismuth molybdates under comparable test conditions (Table 5).

**Table 5.** Comparison of the apparent propene oxidation activation energies for different bismuth molybdates.

Compound	Activation energy ( $\text{kcal mol}^{-1}$ )	Reference
$\gamma\text{-Bi}_2\text{MoO}_6$	43	[43]
$\beta(\text{L})\text{-Bi}_2\text{Mo}_2\text{O}_9$	45	this study
$\beta(\text{H})\text{-Bi}_2\text{Mo}_2\text{O}_9$	41	[44]
$\alpha\text{-Bi}_2\text{Mo}_3\text{O}_{12}$	53	[43]

In this study, it was important to verify that the measured catalytic properties did indeed correspond to pure phases, and also to verify that no superficial transformation occurred after catalytic testing. For this, the solids were characterized by XPS before and after each catalytic test. The spectra obtained for  $\beta(\text{L})\text{-Bi}_2\text{Mo}_2\text{O}_9$ , before and after testing over a wide range of energies, and specifically in the Mo 3d region, are presented in Figs. S7 and S8. The spectral matching results are shown in Table 6. Bismuth is systematically observed in the +3 oxidation state, and molybdenum predominantly in the +6 oxidation state although in some cases, it was slightly reduced to  $\text{Mo}^{5+}$  (Fig. S8). The relative amount of  $\text{Mo}^{5+}$  never exceeded 5% and could not be attributed to any specific event. Within the accuracy limitations of the XPS analyses, the Bi/Mo surface molar ratios were found to correspond relatively well to the bulk ratios. This was not the case for  $\gamma\text{-Bi}_2\text{MoO}_6$ , which exhibits a

higher surface bismuth oxide content. Following catalytic testing, although some minor changes were detected in the spectra, the Bi/Mo ratios remained unchanged.

**Table 6:** XPS analyses of bismuth molybdates before testing as a catalyst in the oxidation of propene. The relative content of Mo<sup>5+</sup> (in atomic %) is indicated in brackets.

Catalyst	Line	Binding energy (eV)		Bi/Mo	
		before testing	after testing	before testing	after testing
$\gamma$ -Bi <sub>2</sub> MoO <sub>6</sub>	3d <sub>5/2</sub>	Mo <sup>6+</sup> : 232.7	Mo <sup>6+</sup> : 232.7	2.84	2.82
	3d <sub>5/2</sub>	Mo <sup>5+</sup> : 231.2 (5%)	Mo <sup>5+</sup> : 231.2 (5%)		
	4f <sub>7/2</sub>	Bi <sup>3+</sup> : 159.3	Bi <sup>3+</sup> : 159.3		
$\beta$ (L)-Bi <sub>2</sub> Mo <sub>2</sub> O <sub>9</sub>	3d <sub>5/2</sub>	Mo <sup>6+</sup> : 232.2	Mo <sup>6+</sup> : 232.2	1.09	1.09
	4f <sub>7/2</sub>	Bi <sup>3+</sup> : 159.2	Bi <sup>3+</sup> : 159.4		
$\beta$ (H)-Bi <sub>2</sub> Mo <sub>2</sub> O <sub>9</sub>	3d <sub>5/2</sub>	Mo <sup>6+</sup> : 232.2	Mo <sup>6+</sup> : 232.2	1.11	1.09
	3d <sub>5/2</sub>	Mo <sup>5+</sup> : 231.0 (5%)			
	4d <sub>5/2</sub>	Bi <sup>3+</sup> : 159.2	Bi <sup>3+</sup> : 159.4		
$\alpha$ -Bi <sub>2</sub> Mo <sub>3</sub> O <sub>12</sub>	3f <sub>7/2</sub>	Mo <sup>6+</sup> : 232.3	Mo <sup>6+</sup> : 232.3	0.73	0.73
	3d <sub>5/2</sub>	Mo <sup>5+</sup> : 231.1 (4%)	Mo <sup>5+</sup> : 231.3 (7%)		
	4f <sub>7/2</sub>	Bi <sup>3+</sup> : 159.2	Bi <sup>3+</sup> : 159.2		

The presence of an excess of bismuth at the surface of  $\gamma$ -Bi<sub>2</sub>MoO<sub>6</sub> has already been observed by other authors, on solids prepared using a different method [46]. This abnormal surface composition, which appears to be related to the synthesis technique used, could explain the low rate of transformation of propene observed with this phase, and more generally the discrepancies observed in various catalytic studies with regard to the ranking of bismuth molybdate catalysts. This explanation is certainly not exhaustive, and the aforementioned discrepancies could also be explained by other phenomena. All attempts to remove the surface excess of bismuth, by washing in various ammonia, HCl or H<sub>2</sub>O<sub>2</sub> solutions, have failed.

The first step of the oxidation reaction, which is the rate determining step at high temperature, is the abstraction of a hydrogen from the propene methyl group. In the case of  $\alpha$ -Bi<sub>2</sub>Mo<sub>3</sub>O<sub>12</sub>, Getsoian et al. have analyzed all possible oxygen sites as recipients of this hydrogen in the

(010) facet proposed to contain the catalytic active sites [7]. They have shown that among these, an oxygen with an equatorial Mo=O bond and located near a bismuth atom was the most favorable H adsorption site. The orbital interactions between the bismuth lone pair electrons and this oxygen destabilize the HOMO and stabilize the LUMO on the molybdate unit, promoting an electron into a Mo–O  $\pi^*$  orbital and converting the Mo<sup>6+</sup>=O<sup>2-</sup> to a Mo<sup>5+</sup>-O<sup>-</sup> configuration. The highly electrophilic oxygen species formed are able to abstract a hydrogen to produce a Mo<sup>5+</sup>-OH and an allyl radical [7].

At this stage of our research, it is difficult to assess and evaluate all possible active sites on  $\beta(L)$ -Bi<sub>2</sub>Mo<sub>2</sub>O<sub>9</sub>. However, it could be postulated that the active sites lie in the (101) plane, exposing a charge-neutral surface and presenting both Bi and Mo centers in close interaction. This plane also has the lowest surface energy of any low-index plane, and is the most exposed plane (Fig. 1). Analysis of the oxygen species in this plane show that one of these exhibits an equatorial Mo(1)=O(4) bond towards which the lone pair electron of a bismuth cation Bi(1) is pointed (Fig. 8). The geometric environment of this oxygen is very similar to that identified as the active site in the  $\alpha$ -Bi<sub>2</sub>Mo<sub>3</sub>O<sub>12</sub> phase with very close Bi-O and Mo=O distances (2.91 and 1.73Å instead of 2.97 and 1.76Å). We propose that this site could be responsible for the abstraction of hydrogen from the methyl group of propene.

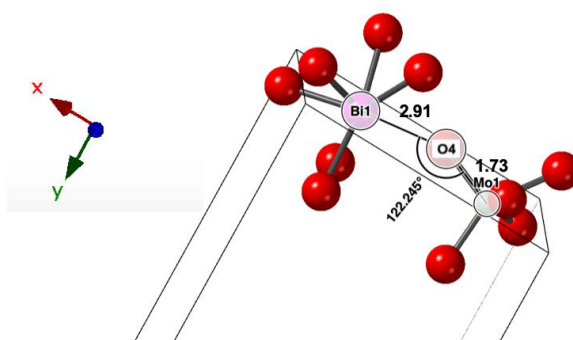


**Fig. 8** Schematic representation of the proposed active site with selected geometries (Å) on the (101) surface of  $\beta(L)$ -Bi<sub>2</sub>Mo<sub>2</sub>O<sub>9</sub>.

The active site density in the (101) facets is more clearly revealed in Fig. 9, which shows that the O4 oxygen is alternately situated above and below the plane. In the figure, the possible active sites on the (101) were represented using a ball and sticks 2D-projection of the atoms constituting these sites and a HAADF-STEM image corresponding to the projection of the structure in the plane considered is proposed as a background. This allowed to better differentiate them from the others and show their distribution i.e. isolation at the surface.

The similarity between the catalytic sites identified on the surface of the  $\beta(\text{L})\text{-Bi}_2\text{Mo}_2\text{O}_9$  and  $\alpha\text{-Bi}_2\text{Mo}_3\text{O}_{12}$  phases could explain the very similar catalytic properties observed for these two phases. As pointed out by Haber et al., turnover frequencies have almost never been calculated for mild oxidation bulk-type catalysts, because active sites are generally difficult to identify, and even harder to count [47]. Nevertheless, in view of the active site density in the (101) facets and the evaluated relative specific surface area corresponding to these facets (82 % of the total surface area), it is possible to compute the turnover frequency, under the reaction conditions used, which is found to be  $1.2 \cdot 10^{-2} \text{ s}^{-1}$ , or  $2.4 \cdot 10^{-2} \text{ s}^{-1}$  if only those sites with O4 pointing out of the plane are considered to be active. At  $420^\circ\text{C}$  this turnover frequency would be equal to 0.6 or  $1.2 \text{ s}^{-1}$ , which is of the same order of magnitude as that reported by Haber et al., for the case of Bi cations on supported bismuth molybdate, which is the only turnover reference for this type of material [47].

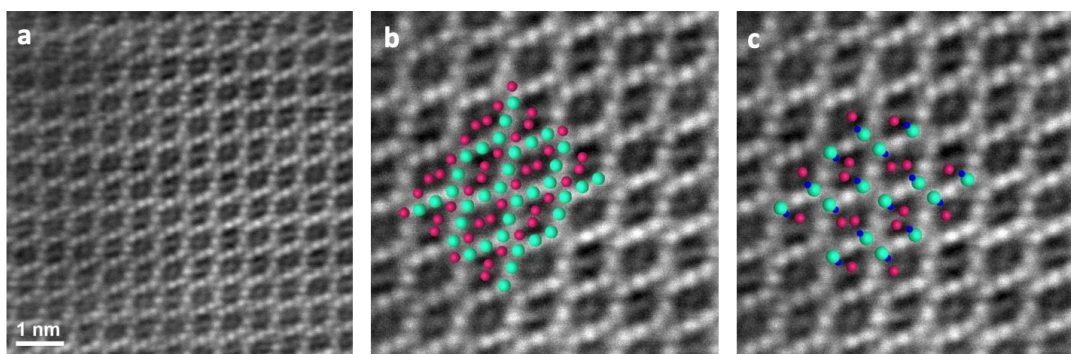


**Fig. 9:** HAADF STEM images of  $\beta(L)$ - $\text{Bi}_2\text{Mo}_2\text{O}_9$  in the (101) direction: a) bare structure, b) with bismuth (green) and molybdenum (red) atoms; c) with Bi(1), Mo(1) and O(4) (blue).

#### 4. Conclusions

Herein, the synthesis and the structure of a new bismuth molybdate, referred as  $\beta(L)$ - $\text{Bi}_2\text{Mo}_2\text{O}_9$  has been described. Despite a very large number of publications dealing with the  $\text{Bi}_2\text{O}_3$ - $\text{MoO}_3$  system, this compound synthesized through the use of a microwave-assisted hydrothermal technique has never been previously reported.

Although it is not yet fully understood why only this technique allows the formation of this new bismuth molybdate phase, we can hypothesize that the rapid rate of temperature increase achieved with microwave assistance allows the reactive species in solution to be stabilized up to synthesis temperature, before being transformed. A different technique that could have allowed similar heating rates to be achieved is the combustion method. However, this approach does not allow the final temperature to be accurately controlled, such that it systematically exceeds that corresponding to the phase stability. The technique described here, which was straightforward to implement and highly reproducible, appears to be efficient not only for the preparation of this new  $\beta(L)$ - $\text{Bi}_2\text{Mo}_2\text{O}_9$  phase, but also for all of the previously known bismuth molybdate phases.

The structure of  $\beta(\text{L})\text{-Bi}_2\text{Mo}_2\text{O}_9$  has completely been solved. It is constructed from  $\text{Mo}_2\text{O}_8$  dimers with discrete  $\text{Bi}_4\text{O}_2$  entities that isolate them from each other. Upon heating up to  $532^\circ\text{C}$ , it undergoes a complete and irreversible transformation to  $\beta(\text{H})\text{-Bi}_2\text{Mo}_2\text{O}_9$ , below which the  $\beta(\text{H})\text{-Bi}_2\text{Mo}_2\text{O}_9$  phase was reported to disproportionate into  $\alpha\text{-Bi}_2\text{Mo}_3\text{O}_{12}$  and  $\gamma\text{-Bi}_2\text{MoO}_6$ .

The catalytic performance of this new phase, in the oxidation of propene to acrolein, has been compared with that of the other known bismuth molybdate phases. The new phase appears to be almost as active, and more selective than  $\alpha\text{-Bi}_2\text{Mo}_3\text{O}_{12}$ , which is the most commonly used active phase of this industrial catalyst. Although the testing of the new phase was time-limited at the scale of a laboratory setup, its analytical properties appear to be very stable. The high activity and selectivity of the phase can be related to the fact that the active sites associating neighboring Bi and Mo cations, should be located in the principal cleavage plane like in the case of  $\alpha\text{-Bi}_2\text{Mo}_3\text{O}_{12}$ . Such feature may not be present for other phases for which active sites are on smaller faces. Our proposed localization of the active site of the new phase was determined by comparing it with the known case of  $\alpha\text{-Bi}_2\text{Mo}_3\text{O}_{12}$ . It would correspond to a molybdenyl  $\text{Mo}=\text{O}$  oxygen in the (101) plane, weakly coordinated with a neighboring bismuth atom. The similarities between this site and that highlighted on  $\alpha\text{-Bi}_2\text{Mo}_3\text{O}_{12}$  could explain the similar catalytic properties observed for these two phases.

## 6. References

[1] P. Mars, D.W. van Krevelen, Oxidations carried out by means of vanadium oxide catalysts, Chem. Eng. Sci. Spec. Suppl. 3 (1954) 41-59.

- [2] J.L. Callahan, R.W. Foreman, F. Veatch, Process for the oxidation of olefins, US 2,941,007, June 10 1957, assigned to Standard Oil Co.
- [3] J.L. Callahan, R.K. Grasselli, E.C. Milberger, H.A. Strecker, Oxidation and ammoxidation of propylene over bismuth molybdate catalyst, *Ind. Eng. Chem. Prod. Res. Dev.* 9 (1970) 134-142.
- [4] B. Grzybowska, J. Haber and J. Janas, Interaction of allyl iodide with molybdate catalysts for the selective oxidation of hydrocarbons, *J. Catal.* 49 (1977) 150-163.
- [5] J.D. Burrington, R.K. Grasselli, Aspects of selective oxidation and ammoxidation mechanisms over bismuth molybdate catalysts, *J. Catal.* 59 (1979) 79-99.
- [6] A.B. Anderson, D.W. Ewing, Y. Kim, R.K. Grasselli, J.D. Burrington and J.F. Brazdil, Mechanism for propylene oxidation to acrolein on  $\text{Bi}_2\text{Mo}_3\text{O}_{12}$ : A quantum chemical study, *J. Catal.* 96 (1985) 222-233.
- [7] A. "Bean" Getsoian, V. Shapovalov, and A.T. Bell, DFT+U Investigation of propene oxidation over bismuth molybdate : Active sites, reaction intermediates, and the role of bismuth, *J. Phys. Chem. C* 117 (2013) 7123-7137.
- [8] G.I. Panov, M.V. Parfenov, E.V. Starokon, A.S. Kharitonov, Investigation of propene oxidation to acrolein by the method of ultralow conversion : A new mechanism of the reaction, *J. Catal.* 368 (2018) 315-323.
- [9] I.K. Kolchin, S.S. Bobkov, L.Ya. Margolis, *Neftekhimiya* 4 (1964) 301-304.
- [10] J.F. Brazdil, D.D. Suresh, R.K. Grasselli, Redox kinetics of bismuth molybdate ammoxidation catalysts, *J. Catal.* 66 (1980) 347-367.
- [11] F. Trifiro, H. Hoser, R.D. Scarle, Relationship between structure and activity of mixed oxides as oxidation catalysts : I. Preparation and solid state reactions of Bi-molybdates, *J. Catal.* 25 (1972) 12-24.

- [12] D. Carson, G. Coudurier, M. Forissier and J.C. Vedrine, Synergy effects in the catalytic properties of bismuth molybdates, *J. Chem. Soc., Faraday Trans.* 79 (1983) 1921-1929.
- [13] A.P.V. Soares, L.D. Dimitrov, M.C-R.A. de Oliveira, L. Hilaire, M.F. Portela, R.K. Grasselli, Synergy effects between  $\beta$  and  $\gamma$  phases of bismuth molybdates in the selective catalytic oxidation of 1-butene, *Appl. Catal. A-Gen.* 253 (2003) 191-200.
- [14] M.T. Le, W.J.M. van Well, P. Stoltze, I. Van Driessche, S. Hoste, Synergy effects between bismuth molybdate catalyst phases (Bi/Mo from 0.57 to 2) for the selective oxidation of propylene to acrolein, *Appl. Catal. A: Gen.* 282 (2005) 189-194.
- [15] Y. Moro-Oka, W. Ueda, Multicomponent Bismuth Molybdate Catalyst: A highly functionalized catalyst system for the selective oxidation of Olefin, in: *Adv. Catal.*, Academic Press, 1994 pp.233-273.
- [16] D. Carson, G. Coudurier, M. Forissier, J.C. Vedrine, A. Laarif, F.J. Theobald, Synergy effects in the catalytic properties of bismuth molybdates, *Chem. Soc., Faraday Trans.* 79 (1983) 1921-1929.
- [17] K. Schuh, W. Kleist, M. Høj, V. Trouillet, P. Beato, A.D. Jensen, J.-D. Grunwaldt, Bismuth molybdate catalysts prepared by mild hydrothermal synthesis : Influence of pH on the selective oxidation of propylene, *Catalysts* 5 (2015) 1554-1573.
- [18] W.J.M. van Well, M.T. Le, N.C. Schiødt, S. Hoste, P.J. Stoltze, The influence of the calcination conditions on the catalytic activity of  $\text{Bi}_2\text{MoO}_6$  in the selective oxidation of propylene to acrolein, *J. Mol. Catal. A : Chem.* 256 (2006) 1-8.
- [19] P. Sprenger, W. Kleist and J.-D. Grunwaldt, Recent advances in selective propylene oxidation over bismuth molybdate based catalysts: Synthetic, spectroscopic, and theoretical approaches, *ACS Catal.* 7 (2017) 5628-5642.
- [20] G. Hidalgo, M. Tonelli, L. Burel, M. Aouine, J.M.M. Millet, Microwave-assisted hydrothermal synthesis, characterization and catalytic performance of  $\text{Fe}_2(\text{MoO}_4)_3$  in the

- selective oxidation of propene, *Catal. Today* 363 (2021) 36-44.
- [21] B. Deniau, G. Bergeret, B. Jouguet, J. L. Dubois, J. M. M. Millet, Preparation of single M1 Phase MoVTe(Sb)NbO Catalyst: Study of the effect of M2 phase dissolution on the structure and catalytic properties, *Top. Catal.* 50 (2008) 33-42.
- [22] M. Aouine, T. Epicier, J.M.M. Millet, In Situ environmental STEM study of the MoVTe oxide M1 phase catalysts for ethane oxidative dehydrogenation, *ACS Catal.* 6 (2016) 4775-4781.
- [23] M. Tonelli, M. Aouine, L. Massin, V. Belliere Baca and J.M.M. Millet, Selective oxidation of propene to acrolein on FeMoTeO catalysts : determination of active phase and enhancement of catalytic activity and stability, *Catal. Sci. Technol.* 7 (2017) 4629-4639.
- [24] M. Tonelli, L. Massin, L. Cardenas, F. Ivars-Barcelo, V. Belliere Baca, J.M.M. Millet, Cooperation between redox couples at the surface of molybdates based catalysts used for the selective oxidation of propene, *J. Catal.* 370 (2019) 412-423.
- [25] M. Lee, S. Sohn and M. Lee, Ionic equilibria and ion exchange of molybdenum(VI) from strong acid solution, *Bull. Korean Chem. Soc.* 32 (2011) 3687-3691.
- [26] C. F. Baes, and R.S. Mesmer, *The Hydrolysis of cations*, John Wiley and Sons, 1976.
- [27] Y.G. Sun, Y.N. Xia, Large-scale synthesis of uniform silver nanowires through a soft, self-seeding polyol process, *Adv. Mater.* 14 (2002) 833-837.
- [28] S. Komarneni, D. Li, B. Newalkar, H. Katsuki, A.S. Bhalla, Microwave-polyol process for Pt and Ag nanoparticles, *Langmuir* 18 (2002) 5959-5962.
- [29] O. Palchik, J.J. Zhu, A. Gedanken, Microwave assisted preparation of binary oxide nanoparticles, *J. Mater. Chem.* 10 (2000) 1251-1254.
- [30] B.A. Cloutt, D.S. Sagatys, G. Smith and R.C. Bott, The preparation and crystal structure of a unique bismuth complex with ethylene glycol : The tris[ethane-1,2-diolato(2-)] dibismuth(III) polymer hydrate, *Aust. J. Chem.* 50 (1997) 947-950.

- [31] S.M. Masoudpanah, S.M. Mirkazemi, S. Shabani, P. Taheri Dolat Abadi, The effect of the ethylene glycol to metal nitrate molar ratio on the phase evolution, morphology and magnetic properties of single phase BiFeO<sub>3</sub> nanoparticles, *Ceram. Intern.* 41 (2015) 9642-9646.
- [32] R.D. Rogers, A.H. Bond and S. Aguinaga, Alcoholysis of bismuth (III) nitrate pentahydrate by polyethylene glycols. Comparison with bismuth (III) nitrate crown ether complexation, *J. Am. Chem. Soc.* 114 (1992) 2960-2967.
- [33] H.Y. Chen and A.W. Sleight, Crystal structure of Bi<sub>2</sub>Mo<sub>2</sub>O<sub>9</sub> : A selective oxidation catalyst, *J. Solid State Chem.* 63 (1986) 70-75.
- [34] F. Theobald, A. Laarif and A.W. Hewat, Redetermination of the crystal structure of a-Bi<sub>2</sub>O<sub>3</sub>-3MoO<sub>3</sub> by neutron diffraction and the catalytic oxidation of propene, *Mat. Res. Bull.* 20 (1985) 653-665.
- [35] A.F. van den Elzen, G.D. Rieck, Redetermination of the structure of Bi<sub>2</sub>Mo<sub>2</sub>O<sub>9</sub> koechlinite, *Acta Crystallogr.* B29 (1973) 2436-2438.
- [36] I. D. Brown, D. Altermatt, Bond-valence parameters obtained from a systematic analysis of the inorganic crystal structure database, *Acta Crystallogr.* B41 (1985) 244-247.
- [37] M. Egashira, K. Matsuo, S. Kagawa, T. Seiyama, Phase diagram of the system Bi<sub>2</sub>O<sub>3</sub>-MoO<sub>3</sub>, *J. Catal.* 58 (1979) 409-418.
- [38] T. Chen, G.S. Smith, The compounds and the phase diagram of MoO<sub>3</sub>-Rich Bi<sub>2</sub>O<sub>3</sub>-MoO<sub>3</sub> system, *J. Solid State Chem.* 13 (1975) 288-297.
- [39] F.D. Hardcastle and I.E. Wachs, Molecular structure of molybdenum oxide in bismuth molybdates by Raman spectroscopy, *J. Phys. Chem.* 95 (1991) 10763-10772.
- [40] I. Matsuura, I.R. Shut and K. Hirakawa, The surface structure of the active bismuth molybdate catalyst, *J. Catal.* 63 (1980) 152-166.

- [41] E.V. Hoefs, J.R. Monnier and G.W. Keulks, The investigation of the type of active oxygen for the oxidation of propylene over bismuth molybdate catalysts using infrared and Raman spectroscopy, *J. Catal.* 57 (1979) 331-337.
- [42] F.D. Hardcastle, I.E. Wachs, Determination of molybdenum-oxygen bond distances and bond orders by Raman spectroscopy, *J. Raman Spectrosc.* 21 (1990) 683-691.
- [43] X. Wu, Y.H. Ng, X. Wen, H.Y. Chung, R. Jien Wong, Yi Du, S.X. Dou, R. Amal, J. Scott, Construction of a  $\text{Bi}_2\text{MoO}_6$ :  $\text{Bi}_2\text{Mo}_3\text{O}_{12}$  heterojunction for efficient photocatalytic oxygen evolution, *Chem. Eng. J.* 353 (2018) 636-644.
- [44] L.D. Krenzke, G.W. Keulks, The catalytic oxidation of propylene: VIII. An investigation of the kinetics over  $\text{Bi}_2\text{Mo}_3\text{O}_{12}$ ,  $\text{Bi}_2\text{MoO}_6$ , and  $\text{Bi}_3\text{FeMo}_2\text{O}_{12}$ , *J. Catal.* 64 (1980) 295-302.
- [45] J.R. Monnier, G.W. Keulks, The catalytic oxidation of propylene : IX. The kinetics and mechanism over  $\beta\text{-Bi}_2\text{Mo}_2\text{O}_9$ , *J. Catal.* 68 (1981) 51-66.
- [46] J.M. Herrmann, J. el Jamal, M. Forissier, Evidence by electrical conductivity for an excess of bismuth at the surface of gamma phase  $\text{Bi}_2\text{MoO}_6$ . Consequence for selectivity in propene catalytic oxidation, *React. Kinet. Catal. Lett.* 37 (1988) 255-260.
- [47] K. Brückman, J. Haber and T. Wiltowski, Active sites for reactions of olefin molecules at surfaces of molybdate catalysts, *J. Catal.* 106 (1987) 188-201.

### Figure caption

**Fig 1** SEM image of the  $\beta(\text{L})\text{-Bi}_2\text{Mo}_2\text{O}_9$  phase.

**Fig. 2** Final Rietveld plot for  $\beta(\text{L})\text{-Bi}_2\text{Mo}_2\text{O}_9$ . The observed data are denoted by blue dot symbols, and the computed ones are represented by the continuous red line. The bottom line corresponds to the difference curve and the blue marks to the Bragg positions.

**Fig. 3** TEM image of a platelet of  $\beta(\text{L})\text{-Bi}_2\text{Mo}_2\text{O}_9$  showing its faceting and the indexed electron diffraction pattern. A fluorite sub-cell is indicated by the dotted lines.

**Fig. 4** Atomic resolution HAADF image of the new phase, along the [110] zone axis (a,b) and the [-2-10] zone axis (c,d) at low-magnification. The indexed electron diffraction patterns (a and c) are shown at high-resolution, with a superimposed view of the computed schematic model (b and d).

**Fig. 5** Projection of the structure of  $\beta(\text{L})\text{-Bi}_2\text{Mo}_2\text{O}_9$  along the  $a$  axis

**Fig. 6** DTA analysis curve of the  $\beta(\text{L})\text{-Bi}_2\text{Mo}_2\text{O}_9$  phase recorded in air ( $10 \text{ mL}\cdot\text{min}^{-1}$ ) at  $5^\circ\text{C}\cdot\text{min}^{-1}$  and new  $\gamma\text{-Bi}_2\text{MoO}_6\text{-MoO}_3$  binary phase diagram.

**Fig 6** DTA analysis curve of the  $\beta(\text{L})\text{-Bi}_2\text{Mo}_2\text{O}_9$  phase recorded in air ( $10 \text{ mL}\cdot\text{min}^{-1}$ ) at  $5^\circ\text{C}\cdot\text{min}^{-1}$ , and new phase diagram of the  $\gamma\text{-Bi}_2\text{MoO}_6\text{-MoO}_3$  binary system.

**Fig. 7:** Raman spectra of the synthesized phases: (a)  $\gamma\text{-Bi}_2\text{MoO}_6$ , (b)  $\beta(\text{L})\text{-Bi}_2\text{Mo}_2\text{O}_9$ , (c)  $\beta(\text{H})\text{-Bi}_2\text{Mo}_2\text{O}_9$  and (d)  $\alpha\text{-Bi}_2\text{Mo}_3\text{O}_{12}$ .

**Fig. 8** Schematic representation of the proposed active site with selected geometries ( $\text{\AA}$ ) on the (101) surface of  $\beta(\text{L})\text{-Bi}_2\text{Mo}_2\text{O}_9$ .

**Fig. 9:** HAADF-STEM images of  $\beta(\text{L})\text{-Bi}_2\text{Mo}_2\text{O}_9$  in the (101) direction: a) bare structure, b) with bismuth (green) and molybdenum (red) atoms; c) with  $\text{Bi}_1$ ,  $\text{Mo}_1$  and  $\text{O}_4$  (blue).